

The Near-Infrared Discrete Extinction Laws of the Galactic Center

DEVAL M. DELIWALA,¹ MATTHEW W. HOSEK JR.,² JESSICA R. LU,³ AND \dots^4

¹*Department of Mathematics, University of California, Berkeley*

²*Department of Physics and Astronomy, University of California, Los Angeles*

³*Department of Astronomy, University of California, Berkeley*

\dots^4

ABSTRACT

A precise, spatially resolved extinction law is essential for interpreting observations of the highly reddened Galactic Center (GC). We use 23,658 red-clump (RC) stars in the *James Webb Space Telescope* NIRCam mosaic of the central $120'' \times 120''$ region (mean $A_{Ks} \approx 2.5$ mag), spanning roughly $1.15\text{-}4.05 \mu\text{m}$. This field is partitioned into concentric annuli centered on Sgr A^* to measure extinction ratios as a function of projected radius. In each annulus, we fit the RC ridge line in the $F115W$, $F140M$, $F182M$, $F212N$, $F323N$, and $F405N$ color-magnitude diagrams using an iterative MCMC procedure that models the RC as a Gaussian-mixture distribution with a linear background. The fitted slopes are converted into extinction ratios relative to $F212N$. Compared to [Fritz et al. \(2011\)](#), the measured ratios are consistent in $F140M$, $F182M$, and $F405N$, but we find significant, radius-dependent deviations at $F115W$ and $F323N$. Specifically, $F115W$ shows deficits at the $3.08\text{-}3.99\sigma$ level in annuli spanning roughly $7.7\text{-}30.9''$ from Sgr A^* , while $F323N$ shows excesses of $3.02\text{-}4.98\sigma$ concentrated in two radial regimes: $13.2\text{-}46.4''$ and $66.2\text{-}81.1''$. These variations demonstrate that adopting region-specific extinctions within the GC is necessary for precision studies of its stellar populations.

1. INTRODUCTION

Understanding how interstellar dust dims and reddens starlight is essential for every area of Galactic and extragalactic astronomy. Distance estimates based on standard candles ([Freedman et al. 2001](#)), stellar mass functions in embedded clusters ([Lada & Lada 2003](#)), and large-scale maps of the Milky Way ([Green et al. 2015](#)) all depend on accurate corrections for wavelength-dependent attenuation. *Extinction* is the combined absorption and scattering of light along the line of sight, and an *extinction law* describes how the extinction magnitude, A_λ , varies with wavelength.

Early work from the optical to the near-infrared (OIR; $0.8\mu\text{m} \lesssim \lambda \lesssim 2.2\mu\text{m}$) showed that A_λ could be approximated by a single power law, $A_\lambda \propto \lambda^{-\beta}$, with β ranging from $\approx 1.5 - 1.8$ based on modest photometric samples ([Rieke & Lebofsky 1985](#); [Draine 1989](#); [Cardelli et al. 1989](#); [Martin & Whittet 1990](#); [Fitzpatrick 1999](#)). This “universal” power law form in the OIR became standard for many years. However, [Martin & Whittet \(1990\)](#) did foreshadow that it would be “remarkable” for a single power-law to be appropriate over an extended wavelength range.

Large surveys have since shown that even in the near-infrared (NIR; $1.15\mu\text{m} \lesssim \lambda \lesssim 4.05\mu\text{m}$), the extinction curve departs from a simple power law. Using 2MASS

photometry, [Froebrich et al. \(2007\)](#) demonstrated that β systematically decreases toward lower Galactic latitudes, making a universal power law of constant β impossible. Later, [Fitzpatrick & Massa \(2009\)](#) leveraged the well determined distance d to the young cluster NGC 6530 to compute $R(V) = A(V)/E(B-V)$ directly from d and the cluster’s absolute magnitude, finding $5.2 \leq R(V) \leq 6.1$. This is substantially lower than the $R(V) \approx 7.0$ inferred by extrapolating a β -power law fit. [Fitzpatrick & Massa \(2009\)](#), using 2MASS and the Advanced Camera for Surveys (ACS) aboard the *Hubble Space Telescope* (HST), introduced a two-parameter analytic model that allows a steepening blueward of $1\mu\text{m}$. [Schlafly et al. \(2016\)](#) used APOGEE spectroscopy with 2MASS photometry to show that optical-mid-IR extinction is well described by a one-parameter family of curves parameterized by $R(V)$, with only modest line of sight variations. Models that adopt a size distribution, with larger grains concentrated in dense clouds and smaller grains in the diffuse ISM, also successfully reproduce the bulk of the observed extinction variations ([Weingartner & Draine 2001](#)). Composite models combining fresh silicates near the Galactic Center (GC) with foreground screens naturally produce curves steeper or flatter than the diffuse-Milky Way baseline, depending

on the small/large grain ratio (Gao et al. 2013; Voshchinnikov et al. 2017).

However, survey-driven studies face two major issues. First, depth limits cause highly-reddened stars to drop below detection thresholds, so bulk fits are dominated by less-reddened foreground stars (e.g., Schultheis et al. 2009). Second, coarse resolution ($\gtrsim 1''$) blends sources in crowded regions, skewing colors where extinction is greatest (e.g., Nogueras-Lara et al. 2021). Both effects are most severe at the GC, where $A_{Ks} \simeq 2.5$ on average and stellar densities exceed 10^7 stars deg $^{-2}$ (e.g., Schödel et al. 2010; Nogueras-Lara et al. 2019).

Consequently, high-resolution, targeted approaches have been pivotal for Galactic Center extinction studies. ISO-SWS and VLT/SINFONI spectroscopy of hydrogen recombination lines in the minispiral (a bright HII region within the central 20'') yield a NIR power law index of $\beta = 2.11 \pm 0.06$ for $\lambda \lesssim 2.8 \mu\text{m}$ (Fritz et al. 2011). Similarly, *HST*/WFC3-IR photometry of 819 red-clump (RC) giants in the GC, combined with 453 proper-motion-selected main-sequence stars in Westerlund 1, reveals an extinction curve both steeper than the diffuse-ISM law and also inconsistent with a single- β power law across the NIR (Hosek et al. 2018, 2019). Also, using high proper-motion stars, Haggard et al. (2024) found a relative L' -band ($\simeq 3.80 \mu\text{m}$) extinction significantly higher than previous studies, which they attribute to stars moving through grain populations local to the GC different from those along the line-of-sight.

JWST has further advanced the field. NIRCam provides 0.031'' resolution in its short-wavelength channels and an exceptional sensitivity to faint, reddened stars (e.g., Schödel et al. 2025). Early JWST extinction-law results outside the GC already demonstrate its potential: RC measurements in 30 Doradus have total-to-selective extinction ratios $A_\lambda/E(F090W - F200W)$ twice the diffuse-MW law beyond 1 μm (Fahrion et al. 2023); pair-matched NIRSpec spectra behind Westerlund 2 show a near-IR slope range $1.5 \leq \beta \leq 2.4$ (Wang & Chen 2024); and color-excess ratios in the Pillars of Creation flatten from $\beta \approx 2.4$ at 1 μm , to $\beta \approx 1.6$ at 4 μm (Li et al. 2024).

One of the foundational methods of deriving the extinction law is the “Red Clump (RC) method,” introduced by Wozniak & Stanek (1996). RC stars are a population of evolved stars in their core-helium burning phase. Their helium-core masses are nearly identical, and in the K-band, their absolute magnitudes depend only on metallicity and age (e.g., Khan et al. 2023). Thus, RC stars serve as reliable infrared standard candles. Assuming a uniform intrinsic color, any color spread on a color-magnitude diagram (CMD) arises pri-

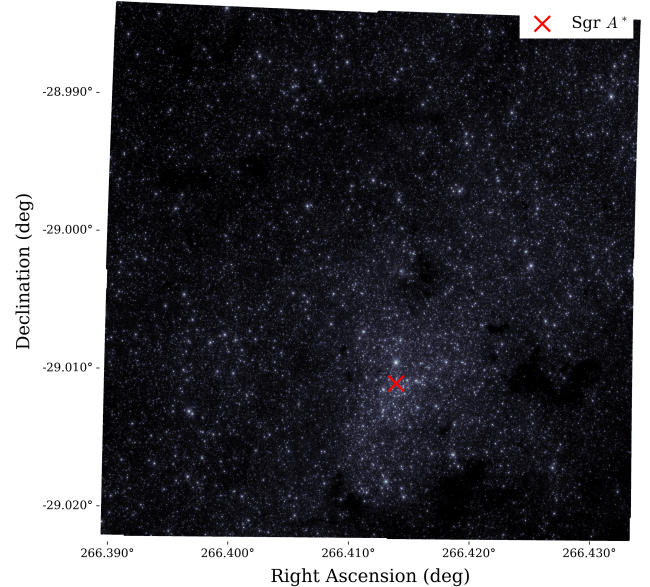


Figure 1. JWST GC field. The red cross indicates Sagittarius A^* .

marily from interstellar extinction. As a result, RC stars are also excellent extinction probes (Gao et al. 2009; Girardi 2016). By analyzing the mean magnitudes and colors of red giant stars (often RC) across different wavelength bands, Messineo et al. (2005); Nishiyama et al. (2009) reported steeper extinctions of $\beta = 1.9$ and 2.0 respectively towards the Galactic Bulge.

This work uses the RC method on JWST NIRCam photometry to (i) measure absolute extinction ratios A_λ/A_{F212N} in concentric annuli centered on Sgr A^* , (ii) assess statistical differences between radial regimes, and (iii) compare our results to existing GC laws (e.g., Nishiyama et al. 2009; Fritz et al. 2011; Hosek et al. 2019; Nogueras-Lara et al. 2020; Haggard et al. 2024). Section 2 outlines the data, Section 3 describes the methodology for measuring A_λ/A_{Ks} extinction ratios, Section 4 presents our results, Section 5 compares our results to known GC laws, and finally, Section 6 summarizes our work.

2. OBSERVATIONS AND MEASUREMENTS

3. METHODS

In a color-magnitude diagram (CMD) the RC cluster appears as a narrow, tilted “bar” at short wavelengths ($\sim 1 - 2 \mu\text{m}$), because every star (roughly) shares the same intrinsic magnitude M_λ and color. The *observed* shifts of those stars are thus driven almost entirely by extinction. The slope of the RC bar in the CMD gives

total-to-selective extinction ratio,

$$R_{\lambda_B} = \frac{A_{\lambda_B}}{E_{\lambda_B - \lambda_R}} = \frac{\partial m_{\lambda_B}}{\partial(m_{\lambda_B} - m_{\lambda_R})},$$

where λ_B and λ_R are the central wavelengths of the bluer and redder filters, respectively. Repeating the fit with the redder m_{λ_R} filter on the vertical axis against the same color yields

$$R_{\lambda_R} = \frac{A_{\lambda_R}}{E_{\lambda_B - \lambda_R}} = \frac{\partial m_{\lambda_R}}{\partial(m_{\lambda_B} - m_{\lambda_R})}.$$

Because both regressions share the same color excess $E_{\lambda_B - \lambda_R} \simeq A_{\lambda_B} - A_{\lambda_R}$ (for RC stars), geometry forces the two slopes to differ by one.

$$R_{\lambda_B} - R_{\lambda_R} = \frac{A_{\lambda_B}}{A_{\lambda_B} - A_{\lambda_R}} - \frac{A_{\lambda_R}}{A_{\lambda_B} - A_{\lambda_R}} = 1. \quad (1)$$

Hence, measuring any single RC slope fixes the other ($R_{\lambda_B} = R_{\lambda_R} + 1$), and their ratio yields the ratio of total extinction:

$$\frac{A_{\lambda_B}}{A_{\lambda_R}} = \frac{R_{\lambda_B}}{R_{\lambda_R}} = \frac{R_{\lambda_R} + 1}{R_{\lambda_R}}. \quad (2)$$

Therefore, measuring the ratio of total extinction $A_{\lambda_B}/A_{\lambda_R}$ reduces to a linear regression and trivial division, a direct consequence of RC geometry in CMD space.

3.1. Concentric Annuli

To measure extinction ratios as a function of distance from Sgr A^* , the observation field is partitioned into concentric annuli. The radial boundaries of these annuli are defined such that each contains a fixed number of RC stars, N . This ensures the measurement procedure defined in Sections 3.2–3.3 remains consistent across the field. Figure 2 shows example annuli for a representative case of $N = 3000$.

3.2. Extracting the Red Clump

Within a given annulus, the RC is first isolated from the surrounding stellar population. To do this, the large extinction difference between $F115W$ and $F212N$ ($A_{F115W}/A_{F212N} \approx 3.63$, Fritz et al. (2011)) is exploited. This makes the RC bar steep and well-defined in $F115W - F212N$ vs. $F115W$ CMDs. To minimize outliers while ensuring ample RC coverage, the unsharp-masking technique described in De Marchi et al. (2016) is used. The CMD is first converted to a Hess Diagram, which represents stellar density as a 2D histogram. Each star's position is modeled as a normal distribution, with its width determined from the associated photometric

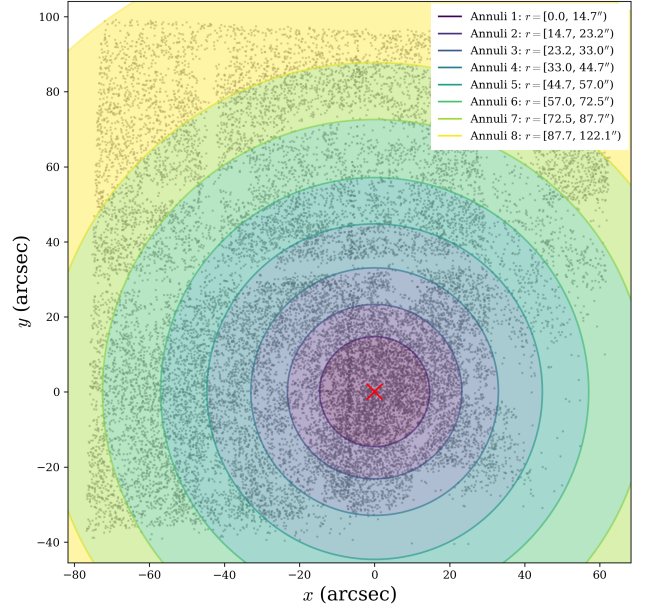


Figure 2. Eight concentric annuli centered on Sgr A^* spanning the GC observation field. RC stars are shown gray. Here, annuli 1–7 contains 3000 RC stars). Annulus 8 contains 2658.

error. The histogram is built with a bin size of 0.02 mags in both color ($F115W - F212N$) and magnitude ($F115W$) space. To generate the unsharp mask, the Hess Diagram is convolved with a 2D Gaussian Kernel with $\sigma = 0.3$ mag in both color and magnitude. The convolved Hess Diagram is then subtracted from the original. Finally, a power-law (gamma) normalization with exponent $\gamma = 1.5$ is applied. Concretely, letting I_{\min} and I_{\max} denote the minimum and maximum pixel values of the *unsharp-masked* Hess diagram in that annulus, each pixel intensity I transforms as

$$I' = \left(\frac{I - I_{\min}}{I_{\max} - I_{\min}} \right)^{\gamma=1.5},$$

which further enhances the contrast of the RC bar relative to the surrounding background. The resulting unsharp mask for $F115W$ - $F212N$ in an example annulus is shown on the right of Figure 3. Afterwards a tight parallel-cutoff is defined by-eye that encloses the RC bar, which is expanded by a factor of three in the *vertical (magnitude)* direction to ensure sufficient coverage (a 2.4 mag vertical RC width in Figure 3). The same selection of stars in this RC zone are “lifted” to all filters analyzed. Stars not present in all filter catalogs— $F115W$, $F140M$, $F182M$, $F212N$, $F323N$, $F405N$ —are dropped. 23,658 RC stars were found across the entire GC observation field.

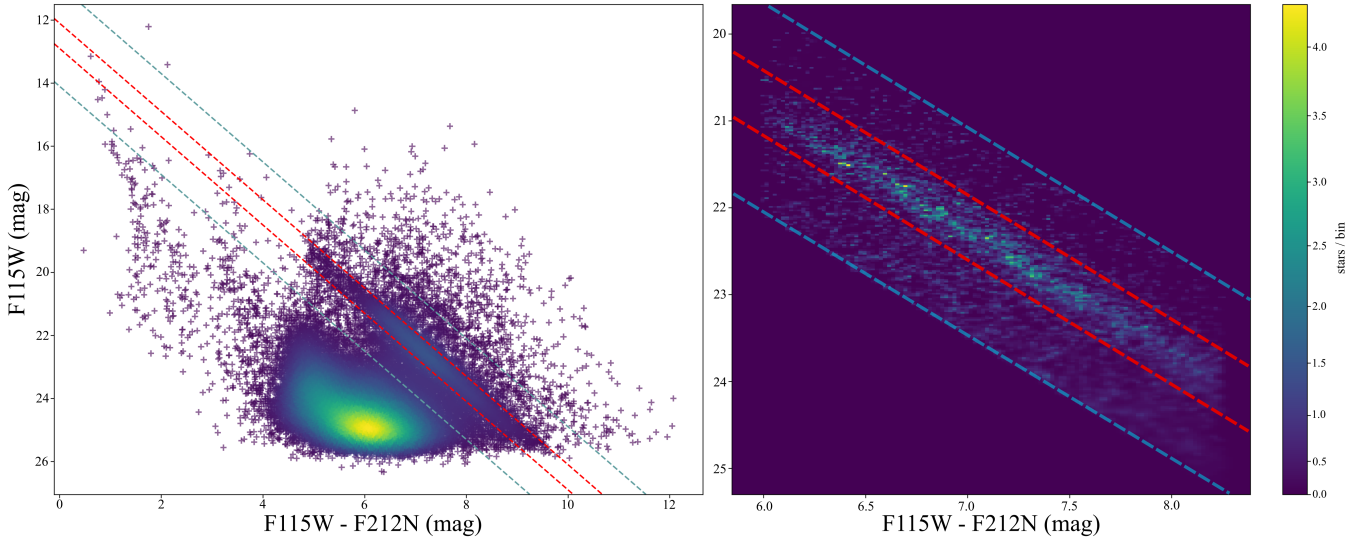


Figure 3. Selection of RC stars in an example annulus. Following De Marchi et al. (2016), the observed CMD (left panel) is converted into a Hess diagram and unsharp masking is applied to isolate the high-density RC ridge; initial by-eye boundaries (red lines) are then drawn around this feature and expanded by a factor of three (blue lines) to ensure comprehensive RC star coverage.

3.3. Red Clump Ridge Curve Fitting

Now that the RC population is isolated across $F115W - F405N$, straight lines are fit to the RC ridge in five CMDs: (i) $F115W - F212N$ vs. $F115W$, (ii) $F115W - F140M$ vs. $F115W$, (iii) $F115W - F182M$ vs. $F115W$, (iv) $F115W - F323N$ vs. $F115W$, (v) $F115W - F405N$ vs. $F115W$.

Similar to the selection of the RC population via the $F115W - F212N$ CMDs in Section 3.2, the RC ridge is fit using $F115W - \lambda$ CMDs because the extinction differential increases most with longer wavelengths relative to $F115W$. The RC is more prominent in these CMDs, yielding tighter constraints on the slope. The total-to-selective extinction ratio

$$\frac{A_{F115W}}{E(F115W - \lambda)}$$

is calculated in each $F115W - \lambda$ CMD, and converted to A_λ/A_{F115W} using Equations 1 and 2. Then ratios

$$\frac{A_\lambda}{A_{F115W}} \implies \frac{A_\lambda}{A_{F212N}}$$

are algebraically derived for all filters $F115W - F405N$.

The choice of $F115W$ on the y -axis is partly arbitrary, but it lies closer to the spectral energy-distribution peak of red-clump giants ($T_{\text{eff}} \sim 4800$ K, $\lambda_{\text{max}} \sim 0.6\mu\text{m}$), so RC stars are intrinsically brighter in that band.

3.3.1. Fitting Straight Lines

The procedure begins by partitioning the RC bar into $n = 10$ contiguous tiles along the color axis, as illustrated in the left panel of Figure 4. Within each tile,

a one-dimensional magnitude histogram is constructed using a bin size of 0.1 mag. This binning width provides an optimal balance between resolving the RC peak and maintaining sufficient counts per bin for robustness. Within each histogram, a compound Gaussian-linear model (Astropy Collaboration et al. 2022) is fit using the emcee MCMC Ensemble sampler (Foreman-Mackey et al. 2013). The Gaussian component captures the RC overdensity and the linear component accounts for the background trend. The measured Gaussian means, representing the RC peaks, remain stable and do not change significantly with smaller bin sizes across any tile histograms. After extracting the mean magnitude from the Gaussian fit in each tile, a linear regression is performed through the $n = 10$ mean magnitudes to measure the full RC slope.

The tiles must lie *orthogonal* to the RC ridge so the MCMC-derived means trace the ridge itself for the final regression. Otherwise each returned mean from vertical tiles would be skewed with the geometric tilt of the RC bar. To accomplish this, the CMD is rotated counter-clockwise by $\theta = \tan^{-1}(m_{\text{ansatz}})$, where m_{ansatz} is the slope of the provisional parallel cutoffs defined in Section 3.2. This rotation renders the RC bar (roughly) horizontal. Then n vertical, contiguous tiles are laid across the full length of the horizontal bar. In this frame, the tiles are orthogonal to the RC ridge. Afterwards everything is un-rotated to the original frame, producing the tiles in the left of Figure 4. This rotation ensures the returned Gaussian mean magnitudes from each tile follow the RC bar itself, without any geometric skew.

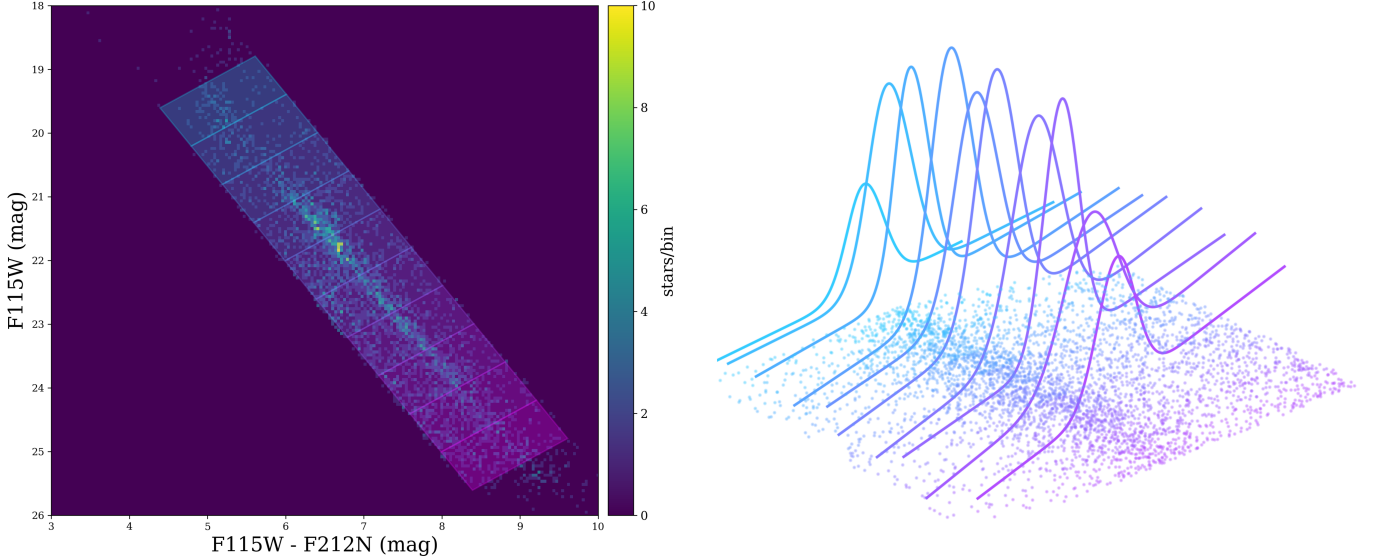


Figure 4. *Left:* Tiles are generated along the RC bar to guide the collective MCMC slope fit. MCMC is used to fit a compound Gaussian-linear model in each tile. *Right:* View of RC fitting with $n = 10$ tiles. The measured Gaussian means from each tile trace out the RC ridge.

Mixture Model—For a single histogram bin center y_i with observed count n_i , a Gaussian approximation to counting statistics with

$$\sigma_i = \sqrt{n_i + 1}$$

is adopted. This is appropriate in the regime where each bin contains many stars; RC slopes were verified to be insensitive to this approximation relative to their uncertainties. The following intensity model is posited:

$$\begin{aligned} \lambda(y_i|\vec{\theta}) &= f_{\text{RC}} a \exp \left[-\frac{1}{2} \left(\frac{y_i - \mu}{\sigma} \right)^2 \right] \\ &\quad + (1 - f_{\text{RC}}) \max(my_i + b, 0), \end{aligned}$$

with parameter vector

$$\vec{\theta} = (u, a, \mu, \sigma, m, b), \quad f_{\text{RC}} = \frac{1}{1 + e^{-u}} \in (0, 1),$$

where

- a, μ, σ describe the Gaussian-component RC peak.
- m, b describe the linear non-RC background trend.
- f_{RC} physically represents the *fraction* of all stars in the tile that belong to the RC component. The logit, $u \in \mathbb{R}$, is sampled rather than f_{RC} itself, so that walker diffusion is unrestricted, instead of sampling a fraction in $[0, 1]$. This also reduces the integrated autocorrelation time described in Section 3.4.

Assuming independent Gaussian noise, the log-likelihood for one tile is

$$\ln \mathcal{L} = -\frac{1}{2} \sum_i \left[n_i - \lambda(y_i|\vec{\theta}) \right]^2 / \sigma_i^2 - \frac{1}{2} \sum_i \ln(2\pi\sigma_i^2).$$

Priors—Weakly informative but physically motivated priors are imposed:

$$\begin{aligned} u &\sim \text{logit-Beta}(\alpha = 3, \beta = 2), \\ a &\sim \mathcal{U}(0, 10^3), \\ \mu &\sim \mathcal{U}(\bar{y} - 2s, \bar{y} + 2s), \\ \sigma &\sim \mathcal{U}(\max\{0, s - 0.5\}, s + 0.5), \\ m &\sim \mathcal{U}(-10, 10), \quad b \sim \mathcal{U}(0, 50), \end{aligned}$$

where \bar{y} and s are the sample mean and standard deviation of the vertical density distribution y . Priors are zero outside the stated intervals, so the overall log-prior is $-\infty$ whenever a walker steps outside these bounds. The values $\alpha = 3, \beta = 2$ reflect the expectation that, within a well-selected tile, a majority of stars may be RC. However, the prior remains fairly broad ($\text{Var}[\text{Beta}(3, 2)] = 0.04$), letting the data dominate whenever there are enough counts. After sampling in the unbounded logit variable u , the Jacobian $\ln[f(1 - f)]$ is used to correctly map back to a Beta(α, β) prior on f_{RC} .

Posterior Sampling—The posterior distribution for a given tile k ,

$$\ln p(\vec{\theta}_k | \text{data}) = \ln \mathcal{L} + \ln p(\vec{\theta}_k),$$

is mapped using the affine-invariant Ensemble sampler from `emcee` (Foreman-Mackey et al. 2013). The sampler is configured with 64 walkers for 15,000 steps, including a 1,000-step burn-in. These values are determined by the autocorrelation analysis detailed in Section 3.4. For each tile $k \in \{1, \dots, n\}$, the posterior medians of the parameters are recorded as

$$\tilde{\mu}_k, \tilde{\sigma}_k, \tilde{a}_k, \tilde{f}_{\text{RC},k}.$$

The posterior standard deviation of the centroid,

$$\sigma_{\mu,k} = \sqrt{\text{Var}_{\text{post}}(\mu_k)},$$

is adopted as the formal uncertainty on the RC position. For each tile k , $\tilde{y}_k \equiv \tilde{\mu}_k$ is taken as the RC centroid in magnitude, and \tilde{x}_k is defined as the median stellar color $x = m_{F115W} - m_\lambda$ of all stars in that tile. The uncertainty in \tilde{x}_k is negligible compared to $\sigma_{\mu,k}$ for the purpose of the final ridge-line-slope in Section 3.3.1.0.

To ensure a robust final fit, only tiles that satisfy $\sigma_{\mu,k} \leq 0.3$ mag, maintain an RC fraction $\tilde{f}_{\text{RC},k} > 0.01$, and meet the autocorrelation criteria defined in Section 3.4 are retained.

Linear Regression—To determine the final extinction ratio, a weighted linear regression is performed through the representative RC centroids (\tilde{x}_k, \tilde{y}_k) from the valid tiles. Because the CMD axes share photometry (e.g. m_{F115W} appears in both y and $x = m_{F115W} - m_\lambda$), this procedure neglects correlated measurement errors between axes. In practice, this approximation does not change the recovered slopes within the quoted uncertainties.

The total integrated RC *area* under the Gaussian component in tile k is

$$\mathcal{A}_k = \tilde{a}_k \tilde{\sigma}_k \sqrt{2\pi}.$$

Define a normalized area weight, $A_k^{\text{norm}} = A_k / \max_j(A_j)$, which scales the contribution of each tile between 0 and 1. Adopting an inverse-variance weighting scheme, tiles where the RC population is intrinsically faint or sparse are further down-weighted by incorporating the RC fraction $\tilde{f}_{\text{RC},k}$. The final weight for tile k is assigned as

$$w_k = A_k^{\text{norm}} \frac{\tilde{f}_{\text{RC},k}}{\sigma_{\mu,k}^2}.$$

This weighting ensures that tiles with a higher density of RC stars and more precise centroids dominate the fit. The linear regression yields the model

$$y \equiv m_{\text{ext}} x + b_{\text{ext}},$$

where m_{ext} and b_{ext} are the fit parameters. The uncertainty on the slope, σ_m , is derived from the covariance matrix C such that $\sigma_m = \sqrt{C_{00}}$. The value $m_{\text{ext}} \pm \sigma_m$ constitutes the final extinction ratio for the given CMD and annulus.

3.4. Autocorrelation Analysis

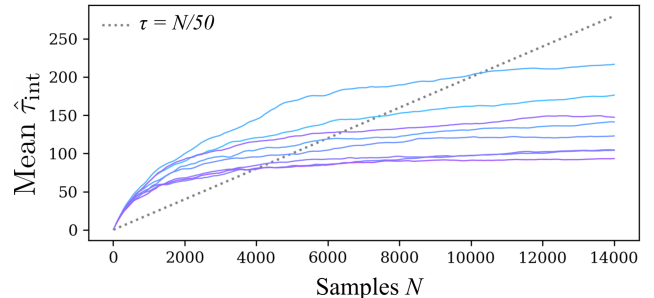


Figure 5. Integrated autocorrelation time $\hat{\tau}_{\text{int}}$ as a function of total samples N for 8/10 CMD tiles that satisfied the uncertainty and $\tilde{f}_{\text{RC},k}$ constraints in Section 3.3.1.0. Each colored curve tracks the mean autocorrelation across all sampled parameters in one tile. The black dashed line denotes the heuristic convergence criterion $\tau = N/50$. Curves that flatten below the dashed line by $N \approx 10^4$ indicate that the 15000 step runs achieve an effective number of independent samples sufficient for reliable posterior estimation.

`emcee`'s Ensemble Sampler yields *correlated* draws, where samples from walks are not statistically independent. A way of quantifying that correlation is via the integrated autocorrelation time

$$\tau_{\text{int}}(m) = 1 + 2 \sum_{s=1}^{\infty} \rho_m(s), \quad \rho_m(s) = \frac{\text{Cov}(\theta_m^{(t)}, \theta_m^{(t+s)})}{\text{Var}(\theta_m)},$$

computed for each parameter θ_m . Intuitively, τ_{int} measures over how many steps the chain “forgets” its past; the *effective* number of independent draws in a run of length N is N/τ_{int} .

While it is not formally possible to guarantee convergence for a nontrivial MCMC, experience with ensemble samplers like emcee shows that a walker whose length satisfies

$$N > 50 \tau_{\text{int}}$$

is typically long enough for a reliable estimation of means and 1σ credible intervals.

$\hat{\tau}_{\text{int}}(N) = \text{mean over parameters}[\tau_{\text{int},m}(N)]$

is monitored as the MCMC runs from Section 3.3.1 progress. The final chain length(s) N is adjusted to exceed $50\tau_{int}$. Figure 5 plots $\hat{\tau}_{int}$ against the number

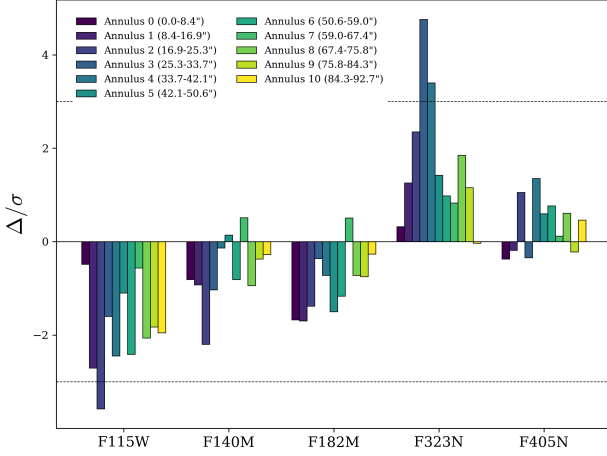


Figure 6. Signed discrepancy Δ_λ of each annulus measurement relative to Fritz et al. (2011) for the fiducial $N_{\text{fb}} = 11$ binning. Dashed lines mark $\pm 3\sigma$. Only $F115W$ (deficits) and $F323N$ (excesses) cross 3σ , and only in specific intermediate-radius annuli.

of samples N for the 8/10 tiles from a CMD whose $\sigma_{\mu,k}$ and $\tilde{f}_{\text{RC},k}$ satisfied the criterion in Section 3.3.1.0.

However, some tiles in some CMDs never satisfy $\hat{\tau}_{\text{int}} < N/50$ even for very long chains, because they contain too few stars. To ensure both per-tile convergence and a robust set of points for the final fit, (i) the number of tiles is fixed to $n = 10$ and (ii) any tile whose sampler still fails $\tau_{\text{int}} \lesssim N/50$ after the run is discarded. This guarantees that every remaining bin meets the autocorrelation criterion while providing enough $(\tilde{x}_k, \tilde{y}_k)$ pairs for linear regression.

4. RESULTS

Table 2 lists the extinction ratios A_λ/A_{F212N} measured in $N_{\text{fb}} = 11$ concentric annuli centered on Sgr A*. The annuli are defined to contain a fixed number of red-clump (RC) stars ($N = 2150$ per annulus), with any remaining outer-field stars excluded. This fiducial binning increases radial resolution while maintaining sufficient counts for robust RC ridge-line fitting in each annulus. Field-averaged ratios and literature comparisons are provided in Table 1. Figure 7 presents the annular ratios as a function of wavelength, together with representative extinction laws for the Galactic Center and the diffuse interstellar medium.

Across annuli, the longest-wavelength ratios ($F140M$, $F182M$, $F405N$) show modest scatter and no evidence for localized radial structure. Relative to Fritz et al. (2011), differences are limited to $F115W$ and $F323N$ and occur only over specific radial ranges.

4.1. Comparison to Fritz et al. (2011)

Table 1. Field-averaged extinction ratios A_λ/A_{F212N} for the $N_{\text{fb}} = 11$ analysis, compared to representative literature laws.

Filter	This study	F11 ^a	N09	NL20	HK18
$F115W$	3.12 ± 0.04	3.63 ± 0.19	3.42	4.12	3.76
$F140M$	2.21 ± 0.04	2.36 ± 0.12
$F182M$	1.25 ± 0.03	1.36 ± 0.08
$F323N$	1.00 ± 0.05	0.64 ± 0.07	0.56	...	0.64
$F405N$	0.41 ± 0.02	0.37 ± 0.06	0.42

^aF11: Fritz et al. (2011). N09: Nishiyama et al. (2009). NL20: Nogueras-Lara et al. (2020). HK18: Hosek et al. (2018, 2020). HG24: Haggard et al. (2024).

NOTE—“This study” values are inverse-variance weighted means over the annuli in Table 2. “...” indicates that the cited law does not provide a value at the corresponding JWST/NIRCam wavelength.

Differences relative to the Fritz et al. (2011) (F11) Galactic Center law are quantified with

$$\Delta_\lambda \equiv \frac{(A_\lambda/A_{F212N}) - (A_\lambda/A_{F212N})_{\text{F11}}}{\sigma_{\text{tot}}},$$

$$\sigma_{\text{tot}}^2 \equiv \sigma_{\text{meas}}^2 + \sigma_{\text{F11}}^2,$$

so that Δ_λ is in units of the combined 1σ uncertainty. Figure 6 plots Δ_λ by annulus and filter for the fiducial $N_{\text{fb}} = 11$ binning.

For the $N_{\text{fb}} = 11$ fixed bins, $|\Delta_\lambda| > 3$ occurs only in $F115W$ and $F323N$. At $F115W$, the measured ratios are lower than F11 in every annulus. The largest difference occurs at $16.9''-25.3''$, where $A_{F115W}/A_{F212N} = 2.73 \pm 0.16$ compared to $(A_{F115W}/A_{F212N})_{\text{F11}} = 3.63 \pm 0.19$, giving $\Delta_{F115W} = -3.58$. The lowest annular ratios occur at $8.4''-16.9''$ (2.80 ± 0.24) and $16.9''-25.3''$ (2.73 ± 0.16), bracketed by a higher inner value at $0''-8.4''$ (3.50 ± 0.19) and higher outer values at $42.1''-92.7''$ ($3.18-3.36$ with $0.27-0.29$ uncertainties; Table 2).

At $F323N$, the differences are not a uniform offset with radius. Inside $25.3''$, the ratios are higher than F11 but remain below 3σ (e.g., 0.69 ± 0.14 at $0''-8.4''$ and 0.92 ± 0.21 at $8.4''-16.9''$, compared to $(A_{F323N}/A_{F212N})_{\text{F11}} = 0.64 \pm 0.07$). The largest excess occurs at $25.3''-42.1''$, with $A_{F323N}/A_{F212N} = 1.20 \pm 0.10$ at $25.3''-33.7''$ ($\Delta_{F323N} = +4.76$) and 1.35 ± 0.20 at $33.7''-42.1''$ ($\Delta_{F323N} = +3.40$). Beyond $42.1''$, the ratios decrease toward $\sim 0.9-1.1$ with larger uncertainties and do not yield additional $>3\sigma$ differences.

4.2. Annulus-to-annulus structure

Radial differences are assessed with pairwise contrasts between annuli,

$$z_{ij}(\lambda) \equiv \frac{(A_\lambda/A_{F212N})_i - (A_\lambda/A_{F212N})_j}{\sqrt{\sigma_i^2 + \sigma_j^2}},$$

$$p_{ij} = 2[1 - \Phi(|z_{ij}|)],$$

where Φ is the standard normal CDF. Figure 8 shows the pairwise matrices for the two filters that consistently produce the strongest radial contrasts across $N_{fb} \in [6, 12]$ ($F115W$ and $F323N$).

At $F115W$, the largest difference is between $0''$ - $8.4''$ and $16.9''$ - $25.3''$, with $z = +3.09$ ($p = 2.0 \times 10^{-3}$). More generally, the largest contrasts involve the $16.9''$ - $25.3''$ annulus and its neighbors, matching the location of the peak deficit in Figure 6.

At $F323N$, the largest difference is between $0''$ - $8.4''$ and $25.3''$ - $33.7''$, with $|z| = 2.95$ ($p = 3.2 \times 10^{-3}$), and the most discrepant cells cluster around the $25.3''$ - $42.1''$ annuli where the $> 3\sigma$ excesses occur. In the remaining filters, annulus-to-annulus contrasts are weaker and show no comparable localized clustering (max $|z| = 2.06$ in $F140M$, 1.82 in $F182M$, and 1.62 in $F405N$), consistent with the small radial scatter visible in Figure 7.

4.3. Robustness to the annulus binning

The analysis is repeated for multiple fixed- N_{fb} annulus definitions spanning $N_{fb} \in [6, 12]$ to test sensitivity to the binning choice. Across all runs, the largest deviations from F11 occur in $F115W$ and $F323N$: the maximum $|\Delta_\lambda|$ per run lies in the ranges 2.96-3.99 at $F115W$ and 3.49-4.98 at $F323N$. The remaining filters remain below $|\Delta_\lambda| \leq 2.20$ at $F140M$, ≤ 1.74 at $F182M$, and ≤ 1.41 at $F405N$.

The radial location of the largest deviations is also stable across binning choices. The most discrepant $F115W$ annulus consistently falls at intermediate radii ($\sim 10''$ - $31''$), and the most discrepant $F323N$ annulus falls at somewhat larger intermediate radii ($\sim 13''$ - $46''$). For the $N_{fb} = 11$ binning, these maxima occur at $16.9''$ - $25.3''$ at $F115W$ and $25.3''$ - $33.7''$ at $F323N$, matching the regimes highlighted in Figures 6 and 8.

5. DISCUSSION

Interestingly, Nogueras-Lara et al. (2020) conclude that the near-IR extinction law shows no significant spatial variation across their survey. They analyze a high angular resolution ($\sim 0.2''$) JHK_s data set spanning ~ 6000 pc 2 and fit a synthetic red-clump model

(Nogueras-Lara et al. 2018) over a grid in power-law index and absolute extinction. Two aspects of that approach naturally suppress sensitivity to small-scale structure: the use of a broad J band ($\lambda \simeq 1.25 \mu\text{m}$), and a $\sim 0.2''$ PSF, which corresponds to $\simeq 0.008$ pc at $R_0 = 8.18$ kpc (Abuter et al. 2019).

JWST/NIRCam resolves much finer structure. The short-wavelength channel samples the sky at $0.031'' \text{ pix}^{-1}$ and is diffraction-limited, with PSF FWHM of $\simeq 0.04''$ at $1.15 \mu\text{m}$ and $\simeq 0.06''$ at $2.12 \mu\text{m}$, corresponding to $\simeq (1.6\text{-}2.4) \times 10^{-3}$ pc at $R_0 = 8.18$ kpc. In addition, the present analysis measures extinction ratios directly from RC ridge slopes in JWST color-magnitude space, and then tests for spatial structure by binning RC stars in projected radius from Sgr A^* (Table 2; Figures 6-8).

Within this framework, the longest-wavelength ratios are mutually consistent across annuli, but two bands show localized radial structure: $F115W$ and $F323N$. At $F115W$, A_{F115W}/A_{F212N} drops from 3.50 ± 0.19 in $0''$ - $8.4''$ to 2.73 ± 0.16 in $16.9''$ - $25.3''$ (a $\simeq 22\%$ decrease), then rises again at larger radii (Table 2). At $F323N$, the ratio increases in $25.3''$ - $42.1''$ and is lower both inside and outside that interval. These effects occur on projected scales well below those effectively probed by the $\sim 0.2''$ -resolution JHK_s analysis of Nogueras-Lara et al. (2020), so the two results are not in tension: the extinction law can be stable on $\gtrsim 0.01$ pc scales while still exhibiting short-wavelength and $3 \mu\text{m}$ structure at $\sim 10^{-3}\text{-}10^{-2}$ pc scales.

The inner-most $0''$ - $8.4''$ annulus does agree with Fritz et al. (2011) in all measured bands. This is expected, as they also measured their extinction ratios in the inner $20'' \times 20''$ region around Sgr A^* .

5.1. Short-wavelength structure

A change in the near-IR slope is naturally interpreted through the Mie size parameter $x \equiv 2\pi a/\lambda$, which sets the transition between small-particle behavior and gray extinction for a characteristic grain radius a (Bohren & Huffman 1983; Draine 2011). A useful reference scale is

$$a_{\text{trans}} \equiv \frac{\lambda}{2\pi} \approx 0.18 \left(\frac{\lambda}{1.15 \mu\text{m}} \right) \mu\text{m}, \quad (3)$$

so the extinction between $F115W$ and $F212N$ is most sensitive to grains in the $a \sim 0.1\text{-}0.3 \mu\text{m}$ range. The depressed A_{F115W}/A_{F212N} in $8.4''$ - $25.3''$ therefore indicates a locally flatter $1.15\text{-}2.12 \mu\text{m}$ reddening vector than in $0''$ - $8.4''$ and beyond $\gtrsim 25.3''$. In grain-population terms, this is consistent with a size distribution weighted toward larger effective radii in that projected radial interval, either through an enhancement of $a \gtrsim a_{\text{trans}}$

Table 2. Extinction ratios A_λ/A_{F212N} measured in $N_{\text{fb}} = 11$ concentric annuli centered on Sgr A*. Each annulus label gives the projected radial range in arcseconds. Uncertainties are 1σ .

Annulus ($r_{\text{in}}-r_{\text{out}}$)	$F115W$	$F140M$	$F182M$	$F323N$	$F405N$
0 (0.0-8.4)	3.50 ± 0.19	2.20 ± 0.16	1.15 ± 0.10	0.69 ± 0.14	0.32 ± 0.11
1 (8.4-16.9)	2.80 ± 0.24	2.16 ± 0.18	1.16 ± 0.09	0.92 ± 0.21	0.35 ± 0.11
2 (16.9-25.3)	2.73 ± 0.16	2.28 ± 0.17	1.19 ± 0.08	0.96 ± 0.25	0.34 ± 0.11
3 (25.3-33.7)	2.92 ± 0.22	2.49 ± 0.24	1.27 ± 0.10	1.20 ± 0.10	0.50 ± 0.11
4 (33.7-42.1)	3.07 ± 0.26	2.40 ± 0.20	1.29 ± 0.09	1.35 ± 0.20	0.41 ± 0.10
5 (42.1-50.6)	3.30 ± 0.28	2.22 ± 0.18	1.25 ± 0.08	1.12 ± 0.28	0.42 ± 0.10
6 (50.6-59.0)	3.34 ± 0.29	2.24 ± 0.19	1.23 ± 0.09	0.98 ± 0.23	0.44 ± 0.11
7 (59.0-67.4)	3.36 ± 0.29	1.97 ± 0.17	1.15 ± 0.10	0.96 ± 0.25	0.39 ± 0.10
8 (67.4-75.8)	3.30 ± 0.28	2.12 ± 0.19	1.20 ± 0.10	0.89 ± 0.23	0.36 ± 0.09
9 (75.8-84.3)	3.18 ± 0.27	2.13 ± 0.19	1.22 ± 0.10	1.01 ± 0.25	0.39 ± 0.10
10 (84.3-92.7)	3.22 ± 0.27	2.18 ± 0.19	1.22 ± 0.10	1.01 ± 0.25	0.39 ± 0.10

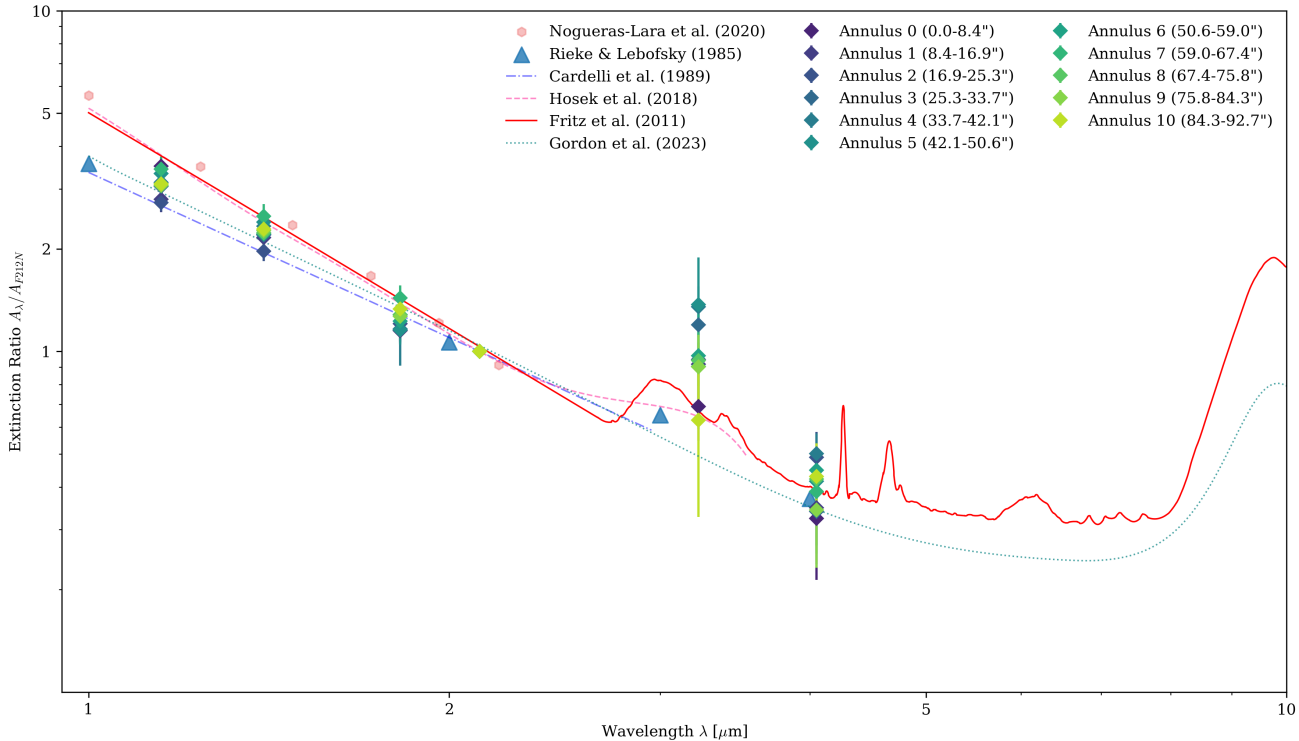


Figure 7. Extinction ratios A_λ/A_{F212N} measured in concentric annuli (colored points with 1σ error bars) compared to representative Galactic Center and diffuse-ISM extinction laws. Laws are rendered with SPISEA (Hosek et al. 2020).

grains or a depletion of smaller grains that normally steepen the near-IR slope (Mathis et al. 1977; Weingartner & Draine 2001). Coagulation in dense gas provides a concrete mechanism for such a shift in the relevant size range (Ossenkopf & Henning 1994; Ormel et al. 2011).

5.2. $3\mu\text{m}$ behavior and The Circumnuclear Disk

The $F323N$ enhancement is confined to $25.3''$ - $42.1''$ (0.98-1.67 pc), where the ratio rises to 1.20 ± 0.10 and 1.35 ± 0.20 before returning toward $\simeq 1.0$ at larger radii

(Table 2). This radial localization overlaps the projected radius of the circumnuclear disk's (CND) inner edge (Harada et al. 2015). Unlike the shorter-wavelength ratios, the $3\mu\text{m}$ window is affected by strong solid-state absorption features in addition to the smooth continuum extinction, most notably the $3.05\mu\text{m}$ H_2O ice band and neighboring hydrocarbon features that can distort a pure power-law behavior (Boogert et al. 2015; Fritz et al. 2011). A natural interpretation is therefore that the annuli intersecting the ~ 1 - 2 pc molecular material

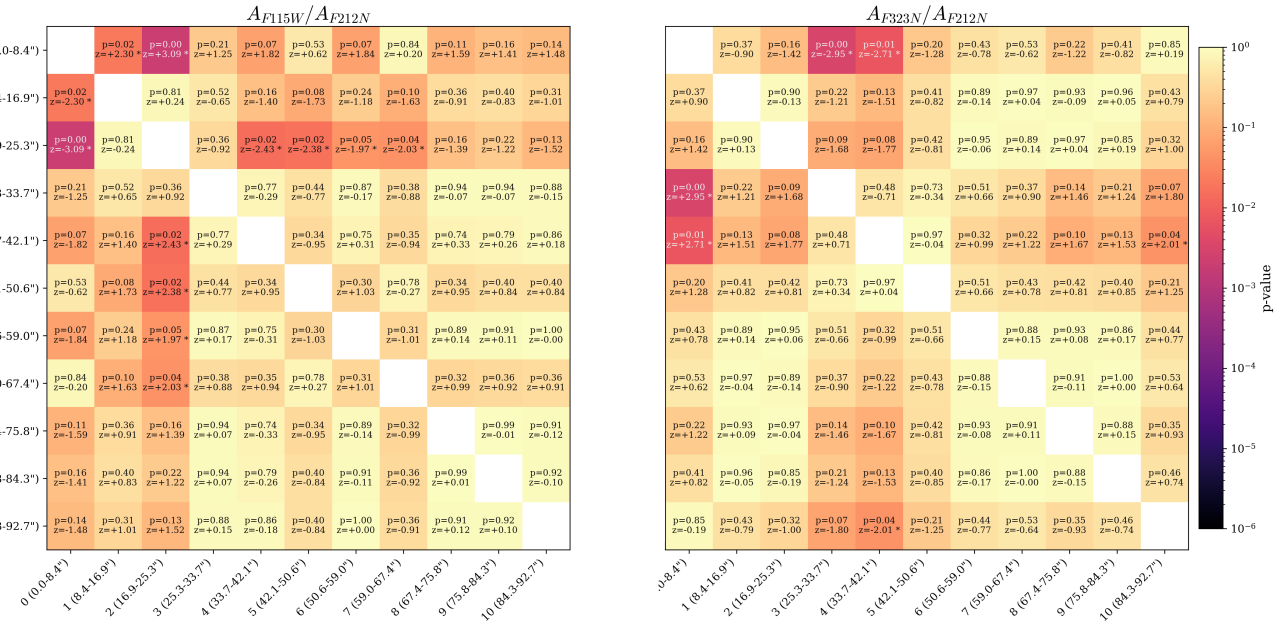


Figure 8. Pairwise annulus contrasts for the two bands that show the strongest, most repeatable departures from F11. Each cell reports the two-sided p -value and the corresponding z -score for $z_{ij} = (R_i - R_j)/\sqrt{\sigma_i^2 + \sigma_j^2}$ with $R \equiv A_\lambda/A_{F212N}$. The clustering of strong contrasts around the same intermediate-radius annuli supports a radius-coherent pattern in $F115W$ and $F323N$, while the other bands remain mutually consistent across annuli.

have systematically different ice-mantle optical depths than the inner $\lesssim 1$ pc lines of sight, producing a localized increase in A_{F323N}/A_{F212N} even when the longer-wavelength continuum ratios remain stable.

5.3. Elsewhere in the Galactic Center

Recent JWST/NIRCam measurements toward Sagittarius C provide an external point of comparison in a different GC environment. Bravo-Ferrés et al. (2025) report $A_{F115W}/A_{F162M} = 1.84 \pm 0.03$ and $A_{F212N}/A_{F162M} = 0.607 \pm 0.014$, which implies $A_{F115W}/A_{F212N} = 3.03 \pm 0.09$ after renormalization. The corresponding renormalized $F405N$ ratio is $A_{F405N}/A_{F212N} = 0.41 \pm 0.03$ from their $A_{F405N}/A_{F162M} = 0.248 \pm 0.017$. Both ratios are consistent with the field-averaged values in Table 1, supporting the overall normalization of the present curve at $F115W$ and $F405N$ m while reinforcing that spatial variations, when present, are most readily exposed at the shortest wavelengths and in the $3\mu\text{m}$ region.

6. CONCLUSION

We measure near-infrared extinction ratios A_λ/A_{F212N} across the central $120'' \times 120''$ JWST/NIRCam mosaic of the Galactic Center using 21,195 red-clump (RC) stars. To test for spatial structure, the mosaic is binned in projected radius from

Sgr A^* using $N_{\text{fb}} = 11$ concentric annuli. The outermost annulus reaches $r \simeq 92.7''$, which is the largest radius fully contained within the $120'' \times 120''$ footprint about Sgr A^* (Table 2). Extinction ratios are measured in each annulus from the RC ridge slopes in JWST color-magnitude space. The method depends only on the observed RC geometry and does not require stellar evolution models, but assumes the RC color spread is dominated by interstellar extinction.

Inverse variance weighted means over the annuli give the field-average ratios

$$\begin{aligned} \frac{A_{F115W}}{A_{F212N}} &= 3.12 \pm 0.04, & \frac{A_{F140M}}{A_{F212N}} &= 2.21 \pm 0.04, \\ \frac{A_{F182M}}{A_{F212N}} &= 1.25 \pm 0.03, & \frac{A_{F212N}}{A_{F212N}} &= 1.00, \\ \frac{A_{F323N}}{A_{F212N}} &= 1.00 \pm 0.05, & \frac{A_{F405N}}{A_{F212N}} &= 0.41 \pm 0.02, \end{aligned}$$

(Table 1). Spatial structure is confined to two bands. At $F115W$, the ratio drops from 3.50 ± 0.19 in $0''-8.4''$ to a minimum of 2.73 ± 0.16 in $16.9''-25.3''$, then rises again at larger radii (Table 2). At $F323N$, the ratio is enhanced in $25.3''-42.1''$ (1.20 ± 0.10 and 1.35 ± 0.20 in the two annuli) and lower both inside and outside that interval. In contrast, $F140M$, $F182M$, and $F405N$ are consistent across annuli within their formal uncertain-

ties, with no comparable radial trends. Pairwise annulus comparisons show the same pattern: the strongest annulus-to-annulus differences occur only in $F115W$ and $F323N$ (Figure 8).

Relative to Fritz et al. (2011) (F11), only $F115W$ and $F323N$ reach $|\Delta_\lambda| > 3$ in the $N_{fb} = 11$ annuli analysis. The largest $F115W$ deficit occurs in $16.9''$ - $25.3''$ ($\Delta_{F115W} = -3.58$), while the largest $F323N$ excesses occur in $25.3''$ - $33.7''$ and $33.7''$ - $42.1''$ ($\Delta_{F323N} = +4.76$ and $+3.40$). The inner-most $0''$ - $8.4''$ annulus agrees with F111 in all measured bands. This is expected, as F11 also measured their extinction ratios in the inner $20'' \times 20''$ region around Sgr A^* . Together, this shows extinction variations are radially localized rather than global offsets.

These results do support a single extinction curve being adequate for 1.40 - $4.05 \mu\text{m}$ work across the full $120'' \times 120''$ mosaic at the present precision. However, location-dependent corrections become important at $1.15 \mu\text{m}$ and in the $3 \mu\text{m}$ window. The radial trends described above refer to projected distance from Sgr A^* within that mosaic, spanning $r = 0''$ - $92.7''$. The $F323N$ excess appears at $25.3''$ - $42.1''$ (0.98 - 1.67 pc), close to the commonly adopted inner radius of the circumnuclear cisk ($r_{in} \simeq 1.5$ pc; $\simeq 30''$) (Harada et al. 2015). If these sight lines intersect more molecular material, additional solid-state opacity near $3 \mu\text{m}$ could raise A_{F323N}/A_{F212N} without changing $F405N$ in the same way (Boogert et al. 2015; Fritz et al. 2011). Overall, the annulus analysis refines the mean Galactic Center extinction law while revealing measurable structure in the extinction curve on sub-parsec scales.

REFERENCES

- Abuter, R., Amorim, A., Bauböck, M., et al. 2019, A&A, 625, L10
- Astropy Collaboration, Price-Whelan, A. M., Lim, P. L., et al. 2022, ApJ, 935, 167
- Benjamin, R. A., Churchwell, E., Babler, B. L., et al. 2003, PASP, 115, 953
- Bohren, C. F., & Huffman, D. R. 1983, *Absorption and Scattering of Light by Small Particles* (New York: Wiley-Interscience)
- Boogert, A. C. A., Gerakines, P. A., & Whittet, D. C. B. 2015, ARA&A, 53, 541
- Bravo-Ferrés, P., van der Marel, N., Underwood, J., et al. 2025, A&A, in press
- Cardelli, J. A., Clayton, G. C., & Mathis, J. S. 1989, ApJ, 345, 245
- De Marchi, G., Panagia, N., Sabbi, E., et al. 2016, MNRAS, 455, 4373
- Draine, B. T. 1989, in ESA SP-290, *Infrared Spectroscopy in Astronomy*, ed. B. H. Kaldeich (Noordwijk: ESA), 93
- Draine, B. T. 2003, ARA&A, 41, 241
- Draine, B. T. 2011, *Physics of the Interstellar and Intergalactic Medium* (Princeton, NJ: Princeton Univ. Press)
- Fahrion, K., Seth, A. C., Bastian, N., et al. 2023, A&A, 671, L14
- Fitzpatrick, E. L. 1999, PASP, 111, 63
- Fitzpatrick, E. L., & Massa, D. 2007, ApJ, 663, 320
- Fitzpatrick, E. L., & Massa, D. 2009, ApJ, 699, 1209
- Foreman-Mackey, D., Hogg, D. W., Lang, D., & Goodman, J. 2013, PASP, 125, 306
- Freedman, W. L., Madore, B. F., Gibson, B. K., et al. 2001, ApJ, 553, 47
- Fritz, T. K., Gillessen, S., Dodds-Eden, K., et al. 2011, ApJ, 737, 73
- Froebrich, D., Murphy, G. C., Smith, M. D., et al. 2007, MNRAS, 378, 1447
- Gao, J., Jiang, B. W., & Li, A. 2009, ApJ, 707, 89
- Gao, J., Jiang, B. W., & Li, A. 2013, ApJ, 776, 7
- Girardi, L., Bressan, A., Bertelli, G., & Chiosi, C. 2001, A&AS, 141, 371
- Girardi, L. 2016, ARA&A, 54, 95
- Ginsburg, A., Barnes, A. T., Battersby, C. D., et al. 2023, ApJ, 959, 36
- Goodman, J., & Weare, J. 2010, Commun. Appl. Math. Comput. Sci., 5, 65
- Gordon, K. D., Clayton, G. C., Decleir, M., et al. 2023, ApJ, 950, 86
- Green, G. M., Schlafly, E. F., Finkbeiner, D. P., et al. 2015, ApJ, 810, 25
- Haggard, Z., Ghez, A. M., Sakai, S., et al. 2024, AJ, 168, 166
- Harada, N., Riquelme, D., Viti, S., et al. 2015, A&A, 584, A102
- Hosek, M. W., Jr., Lu, J. R., Anderson, J., et al. 2018, ApJ, 855, 13
- Hosek, M. W., Jr., Lu, J. R., Anderson, J., et al. 2019, ApJ, 870, 44
- Hosek, M. W., Jr., Lu, J. R., Lam, C. Y., et al. 2020, AJ, 160, 143
- Khan, S., Anderson, R. I., Miglio, A., Mosser, B., & Elsworth, Y. P. 2023, A&A, 680, A105

- Lada, C. J., & Lada, E. A. 2003, *ARA&A*, 41, 57
- Li, A., Chu, Y.-H., Stahl, O., et al. 2024, *ApJL*, 968, L26
- Martin, P. G., & Whittet, D. C. B. 1990, *ApJ*, 357, 113
- Mathis, J. S., Rumpl, W., & Nordsieck, K. H. 1977, *ApJ*, 217, 425
- Messineo, M., Habing, H. J., Menten, K. M., et al. 2005, *A&A*, 435, 575
- Minniti, D., Lucas, P. W., Emerson, J. P., et al. 2010, *New Astron.*, 15, 433
- Nishiyama, S., Tamura, M., Hatano, H., et al. 2009, *ApJ*, 696, 1407
- Nogueras-Lara, F., Gallego-Calvente, A. T., Dong, H., et al. 2018, *A&A*, 610, A83
- Nogueras-Lara, F., Schödel, R., Gallego-Calvente, A. T., et al. 2019, *A&A*, 631, A20
- Nogueras-Lara, F., Schödel, R., Neumayer, N., et al. 2020, *A&A*, 641, A141
- Nogueras-Lara, F., Schödel, R., Dong, H., et al. 2021, *A&A*, 654, A81
- Ossenkopf, V., & Henning, T. 1994, *A&A*, 291, 943
- Ormel, C. W., Min, M., Tielens, A. G. G. M., et al. 2011, *A&A*, 532, A43
- Rieke, G. H., & Lebofsky, M. J. 1985, *ApJ*, 288, 618
- Schlafly, E. F., Schlegel, D. J., Green, G. M., et al. 2016, *ApJ*, 821, 78
- Schödel, R., Najarro, F., Muzic, K., & Eckart, A. 2010, *A&A*, 511, A18
- Schödel, R., Nogueras-Lara, F., Mauerhan, J., et al. 2025, arXiv:2310.11912
- Schlüter, M., Robin, A. C., Reylé, C., et al. 2009, *A&A*, 495, 157
- Voshchinnikov, N. V., Il'in, V. B., Henning, T., & Akhtemov, Z. S. 2017, *A&A*, 605, A40
- Wang, S., & Chen, X. 2024, *ApJL*, 964, L3,
- Weingartner, J. C., & Draine, B. T. 2001, *ApJ*, 548, 296
- Wozniak, P. R., & Stanek, K. Z. 1996, *ApJ*, 464, 233